

## Article

# Degradation Studies of Air-Exposed Black Phosphorous and Black Arsenic Phosphorous

Usman O. Abu <sup>1</sup>, Dinushika Vithanage <sup>2</sup>, Ashan Vitharana <sup>2</sup> , Jacek B. Jasinski <sup>1,\*</sup>  and Gamini Sumanasekera <sup>2,\*</sup><sup>1</sup> Conn Center for Renewable Energy Research, University of Louisville, Louisville, KY 40292, USA<sup>2</sup> Department of Physics and Astronomy, University of Louisville, Louisville, KY 40292, USA

\* Correspondence: jacek.jasinski@louisville.edu (J.B.J.); gamini.sumanasekera@louisville.edu (G.S.)

**Abstract:** This work investigates the effects of oxygen and humidity on black phosphorous (BP) and black arsenic phosphorous ( $As_xP_{1-x}$ ) flakes using Raman spectroscopy and in situ electric transport measurements (four-probe resistance and thermoelectric power, TEP). The results show that the incorporation of arsenic into the lattice of BP renders it more stable, with the degradation times for BP,  $As_{0.2}P_{0.8}$ , and  $As_{0.4}P_{0.6}$  being 4, 5, and 11 days, respectively. The P-P Raman peak intensities were determined to decrease with exposure to oxygen and moisture. The TEP measurements confirmed that both BP and  $As_xP_{1-x}$  are p-type semiconductors with the TEP of  $As_{0.4}P_{0.6}$  stabilizing more slowly than that of BP. In addition, the four-probe resistance of BP and  $As_xP_{1-x}$  stabilized significantly faster when exposed to air after being degassed in a vacuum. This was attributed to the charge transfer between the oxygen redox potential of air and the Fermi energy ( $E_F$ ) of the semiconductors.

**Keywords:** black phosphorous; black arsenic phosphorous; degradation; Raman spectroscopy; electrical transport measurements; in-situ; charge transfer; environmental stability



**Citation:** Abu, U.O.; Vithanage, D.; Vitharana, A.; Jasinski, J.B.; Sumanasekera, G. Degradation Studies of Air-Exposed Black Phosphorous and Black Arsenic Phosphorous. *ChemEngineering* **2023**, *7*, 18. <https://doi.org/10.3390/chemengineering7020018>

Academic Editor: Alirio E. Rodrigues

Received: 9 November 2022

Revised: 15 February 2023

Accepted: 28 February 2023

Published: 3 March 2023



**Copyright:** © 2023 by the authors. Licensee MDPI, Basel, Switzerland. This article is an open access article distributed under the terms and conditions of the Creative Commons Attribution (CC BY) license (<https://creativecommons.org/licenses/by/4.0/>).

## 1. Introduction

Environmental stability is one of the key issues in the development of functional materials, especially when these materials are designed for applications and devices requiring direct environmental exposure. The importance of material stability cannot be overstated as it directly affects the reliability and lifetime of devices they are used in. Understanding of the processes that occur at the interface between materials and the environment, i.e., the processes that are potentially responsible for material degradation is therefore essential. Among such processes are the phenomena occurring at the surface of the material during its exposure to humid air. While in metals this often can lead to a corrosion, such exposure can also significantly affect semiconductors, which are another technologically important class of materials.

The exceptional properties exhibited by black phosphorous (BP) have motivated research into mitigating the effects of its instability [1]. The surface of BP is reactive in air due to the lone pair of electrons a phosphorous atom possesses [2–4]. A photo-assisted reactive oxygen species (ROS) forms and bonds on BP surface upon exposure to ambient environment in the presence of light [5]. A thin layer of hydrophilic oxidized phosphorous ( $P_xO_y$ ) is formed on the surface as it is oxidized [2]. Oxidized regions on the surface of BP appear as small bumps [6] which further react with moisture in air to form etching phosphoric acids [2,4–7] that appear as large droplets [6]. Favron et al. reported that visible light alone induces no degradation on BP [6]; rather, the photo-induced degradation is activated by air or the mixture of air and water. Passivation strategies that have been proposed and tested for the inhibition of degradation in BP can broadly be classified into encapsulation methods and covalent modification methods [4,8,9]. Encapsulation involves coating BP sheets with non-covalent environmentally stable materials that isolate BP from interacting with air. Atomic layer deposition (ALD) is an encapsulation method where

$\text{Al}_2\text{O}_3$ ,  $\text{SiO}_2$ ,  $\text{TiO}_2$  have been used to coat BP layers resulting in long-term stability upon exposure [8,10–12]. In addition, dry transfer methods involving stacking up BP layers with other Table S2 materials such as graphene, hexagonal boron nitride (h-BN),  $\text{MoS}_2$ , etc. [4,9,13], yield stable BP heterostructures with impressive stability. Nevertheless, this method is expensive, sophisticated, and requires a long time to complete.

Covalent modifications or functionalization of BP is achieved when functional groups react with the lone pairs of electrons in phosphorous atoms to yield P-X bonds [4]. The newly formed surface is thus immune from oxygen attacks. Covalent modification can be complicated as they require a trade-off between ensuring stability and preserving the desired properties of phosphorene [8]. Selection of elements from the same group as P or adjacent in the periodic table can help to mitigate this limitation. Yang et al. stabilized BP for 21 days by doping it with Te [14]. They reported that Te doping induced a shift of the conduction band minimum (CBM) of BP so that it approached or went below the redox potential of  $\text{O}_2/\text{O}_2^-$ . In addition, such doping reduced the light-induced  $\text{O}_2$  generation; thus, it inhibits the oxidation process. Recently, exceptional electrical transport properties have been reported for As-doped BP [15]. Based on those previous reports, we hypothesize that the doping (isovalent substitution) of P with much more stable As which can have the same orthorhombic crystal structure as BP [16,17] will yield a more stable alloy with the same structure and similar properties as phosphorene. The As doping not only preserves BP's orthorhombic crystal structure and in-plane anisotropy, but also tunes electronic and optical properties of the material for more applications. The resulting black arsenic-phosphorous ( $\text{As}_x\text{P}_{1-x}$ ), like BP, also has a puckered honeycomb crystal structure with its lattice parameters following approximately the Vegard's law [18], i.e., changing almost linearly with alloy's composition [15,16]. The lattice parameters of  $\text{As}_x\text{P}_{1-x}$  are relatively larger compared to those of BP because the As–As bond length is larger than that of the P–P bond (2.48 Å vs. 2.21 Å in elemental arsenic compared to elemental phosphorous) and substituted As atoms in BP are slightly displaced outwards resulting in the increase in rectangular primitive cell constants of  $\text{As}_x\text{P}_{1-x}$  [19].

Here, we present direct experimental evidence based on Raman spectroscopy and in situ environmental electrical measurements that the introduction of arsenic atoms into BP lattice can enhance its stability. In addition, we discuss and compare the stability of these materials, i.e., BP and  $\text{As}_x\text{P}_{1-x}$ , using a similar mechanism to the one proposed previously for diamond [20] and other semiconductor-type carbon materials [21], where electrochemical charge transfer occurs between the adsorbed water and the surface of semiconductor material exposed to humid air. Better understanding of such processes in BP and  $\text{As}_x\text{P}_{1-x}$  can lead to better protection strategies, as well as to designs of more durable materials.

## 2. Materials and Methods

### 2.1. Synthesis of Black Phosphorous and $\text{As}_x\text{P}_{1-x}$

BP and  $\text{As}_x\text{P}_{1-x}$  ( $x = 0.2, 0.4$  and  $0.6$ ) were synthesized via the chemical vapor transport route (CVT). For the synthesis of BP, red phosphorous (500 mg, Sigma, > 97%) was used as the precursor, while Sn (20 mg, Alfa Aesar, 99.8%) and  $\text{SnI}_4$  (20 mg, Alfa Aesar, 95%) served as transport agents. Red phosphorous, Sn, and  $\text{SnI}_4$  were loaded in a quartz ampoule that was sealed at  $10^{-6}$  Torr. The sealed ampoule was then annealed at 615 °C in two-zone furnace where a temperature gradient of 50 °C was maintained and starting materials were placed at the hot end. Detailed steps for this process have been provided [22–24]. At the same time, stoichiometric amounts of red phosphorus and gray arsenic (Sigma, >97%) were measured into quartz ampoules alongside transport agents, sealed at the same vacuum as BP and annealed at 650 °C with the same temperature gradient maintained in the furnace for the synthesis of  $\text{As}_x\text{P}_{1-x}$  compounds.

## 2.2. Raman Spectroscopy

BP and two compositions of  $\text{As}_x\text{P}_{1-x}$  ( $x = 0.2$  and  $0.6$ ) were crushed to approximately  $10\ \mu\text{m}$  and placed on marked glass slides. Before the Raman spectra of crushed samples were quickly measured, the Raman shift of silicon ( $520\ \text{cm}^{-1}$ ) was used to calibrate the equipment. This was performed for subsequent measurements to avoid shifts in the spectra caused by poor calibration. The glass slides bearing the samples were then placed in an open bath that had a digital hygrometer placed beside it. The average relative humidity and temperature for this experiment were  $35 \pm 5\%$  and  $25\ ^\circ\text{C}$ , respectively. The Raman spectrum for each sample was measured every day to study their systematic degradation until they ultimately degraded. While the total degradation of the samples occurred at different times, it required 19 days to conclude this experiment.

## 2.3. Electrical Transport Measurements

The in situ thermoelectric power (TEP) and four-probe resistance of BP were measured by positioning two small thermocouples (Chromel (KP)/Alumel) and two current leads on a  $4\ \text{mm}$  by  $4\ \text{mm}^2$  BP sample with the aid of small silver epoxy [15,25]. An edge of the sample was fitted on an aluminum plate with a resistive heater ( $\sim 100\ \Omega$ ) beneath. The sample holder carrying the sample and electrical leads were put in a quartz reactor and pumped with a turbomolecular pump down to  $10^{-7}$  Torr. TEP and resistance were measured carefully in real time as the sample was heated gently from room temperature up to  $560\ \text{K}$  and kept at this temperature for 12 h. The sample was then cooled to room temperature for 3 h and exposed to ambient conditions for 72 h. This procedure was replicated for  $\text{As}_{0.4}\text{P}_{0.6}$  and obtained results were analyzed. The setup for the explained process is illustrated in Figure 1.

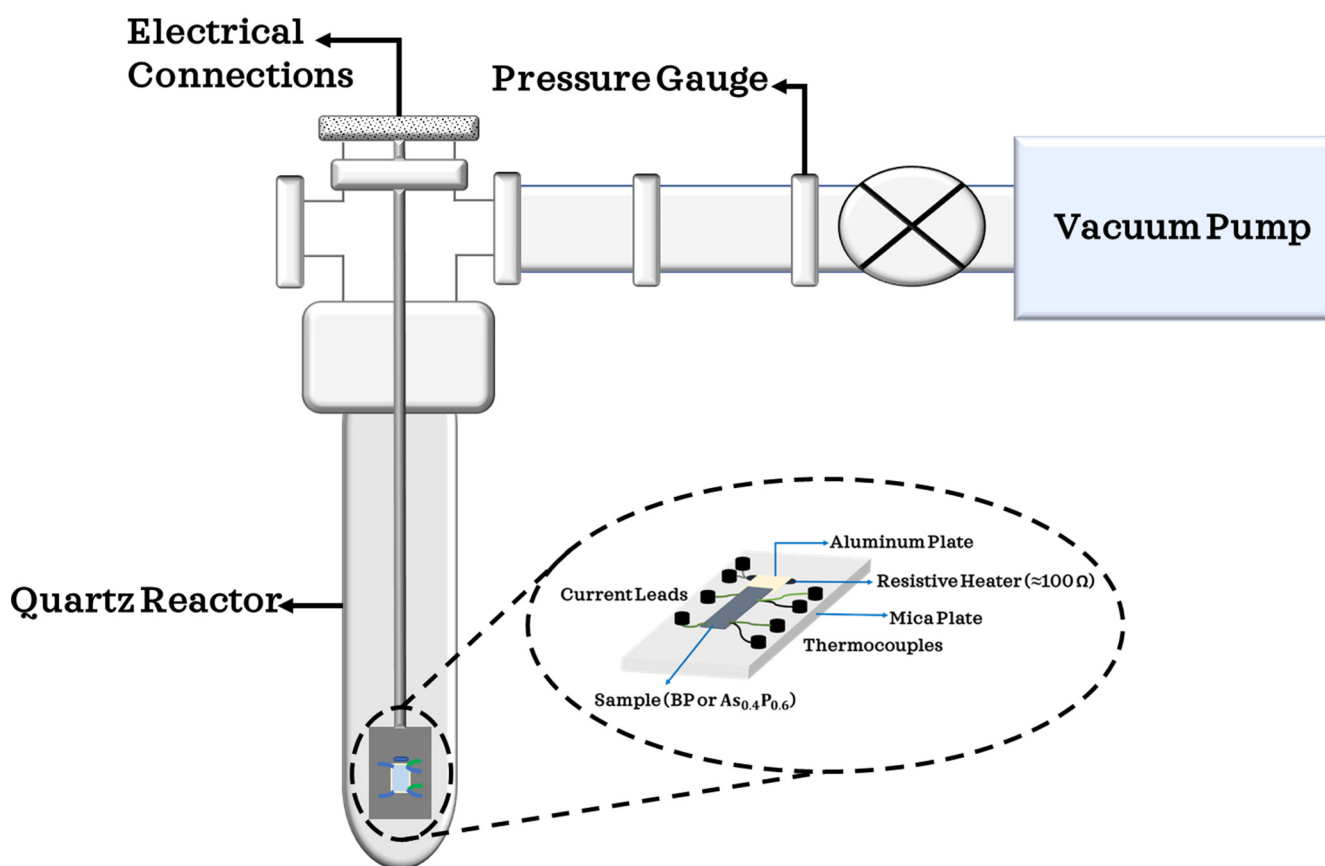


**Figure 1.** Experimental set-up for electrical transport measurements showing the reactor with provisions for pumping and air exposures and the sample probe and the electrical contacts.

### 3. Results and Discussion

#### 3.1. Raman Spectroscopy

The Raman spectra of unexposed synthesized samples are shown in Figure 2. BP shows its signature vibration modes centered at 357, 432 and 460  $\text{cm}^{-1}$  and are assigned the notations  $A_g^1$ ,  $B_{2g}$  and  $A_g^2$  [22,24–26], respectively.  $\text{As}_x\text{P}_{1-x}$  alloys typically exhibit three regimes of Raman vibration modes [15]. There are three As–As vibration modes detected between 200 and 300  $\text{cm}^{-1}$ , two As–P modes that appear between 300– and 30  $\text{cm}^{-1}$  while, similar to BP, three P–P vibration modes appear between approximately 330 and 500  $\text{cm}^{-1}$ . The notations for the As–As modes are also  $A_g^1$ ,  $B_{2g}$  and  $A_g^2$ , respectively.

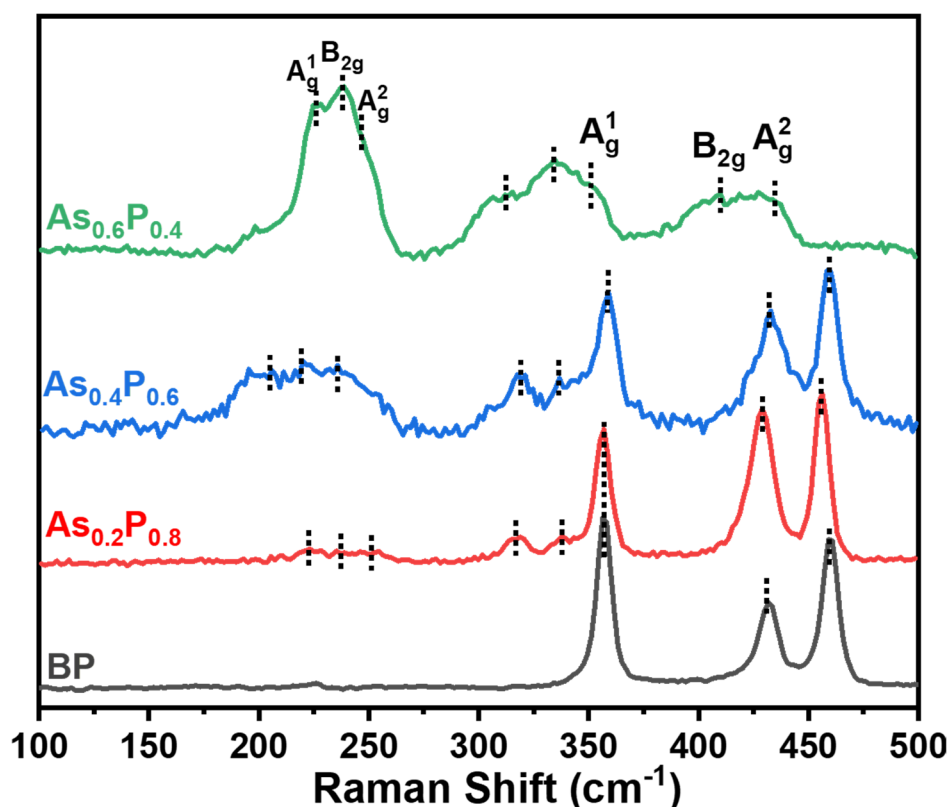


**Figure 2.** Raman spectra of unexposed synthesized pristine BP and  $\text{As}_x\text{P}_{1-x}$  alloys with three different chemical compositions.

The Raman spectra for BP and  $\text{As}_x\text{P}_{1-x}$  alloys measured after continuous exposure to air are presented in Figure 3. BP (Figure 3a), expectedly, degraded faster relative to  $\text{As}_x\text{P}_{1-x}$  alloys (Figure 3b,c). Similarly, Figure S1 shows that the P–P vibration modes for BP quenched faster than those of  $\text{As}_{0.2}\text{P}_{0.8}$ . BP is susceptible to photo-assisted oxidation which causes it to degrade and adversely affects its electronic and optical properties. The degradation of BP is only mildly inhibited by low concentrations of As in  $\text{As}_{0.2}\text{P}_{0.8}$  (Figure 3b). On the other hand,  $\text{As}_{0.6}\text{P}_{0.4}$  (Figure 3c) showed much better stability as it was able to inhibit oxygen attacks for a much longer period. While it required BP 9 days to degrade totally,  $\text{As}_{0.2}\text{P}_{0.8}$  and  $\text{As}_{0.6}\text{P}_{0.4}$  fully degraded after 11 and 19 days, respectively. It is noteworthy to mention that the samples studied in this experiment were all multi-layered. One of the evidences of degradation in multi-layered BP is the blueshift of its Raman peak positions [27] (Figure S3) as a result of the loss of layers as phosphoric acids etch the material top-down [6,8]. The kinetics of oxidation of BP and  $\text{As}_x\text{P}_{1-x}$  were further analyzed by fitting the normalized total Raman intensity for each sample as shown in Figure 3d. The fitted curves correspond to a monoexponential decay function,  $\exp\left(\frac{-t}{\tau}\right)$ .

The decay function parameters are presented in Table S1. It can be inferred that BP decays almost three times faster than  $\text{As}_{0.6}\text{P}_{0.4}$ .

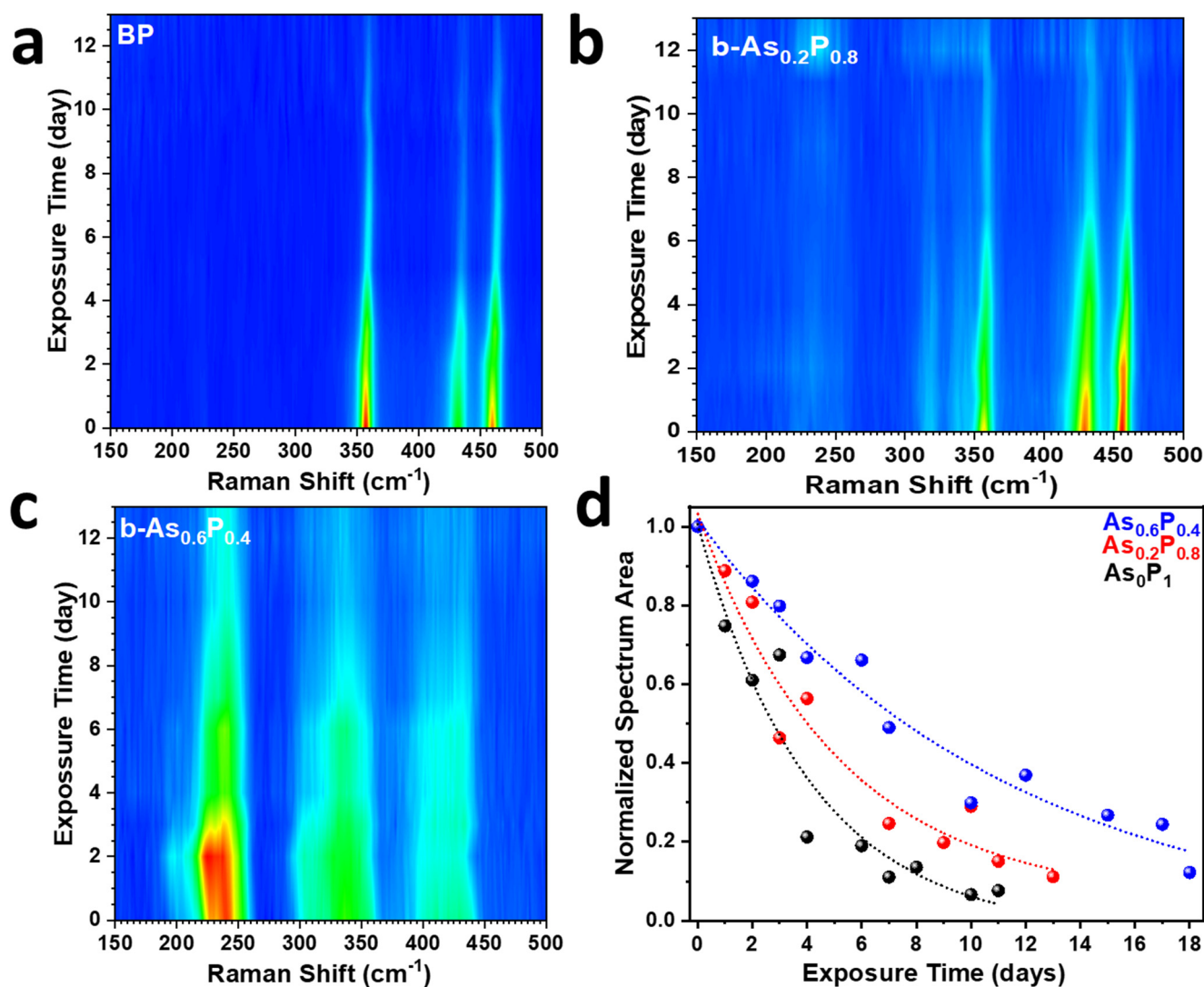


**Figure 3.** Results derived from Raman spectroscopy. (a–c) Degradation maps showing time evolution of Raman spectra upon exposure to ambient environment for BP,  $\text{As}_{0.2}\text{P}_{0.8}$ , and  $\text{As}_{0.6}\text{P}_{0.4}$ , respectively. (d) The total Raman intensity as a function of exposure time for BP ( $\text{As}_0\text{P}_1$ ),  $\text{As}_{0.2}\text{P}_{0.8}$  and  $\text{As}_{0.6}\text{P}_{0.4}$ . The initial ( $t = 0$ ) total intensity for all three samples was normalized to 1.

Since the oxidation of BP is a chemical process, it makes sense to use a chemical approach to inhibit it. Figure S2 shows the relatively fast quenching of P-P Raman peak intensities for BP and  $\text{As}_{0.2}\text{P}_{0.8}$  relative to  $\text{As}_{0.6}\text{P}_{0.4}$ . This shows that alloying BP with high concentration of As limits the possibility of light-induced  $\text{O}_2$  generation and abating the oxidation process [8,14].

### 3.2. In situ Transport Property Measurements of BP and $\text{As}_{0.4}\text{P}_{0.6}$

The normalized TEP for  $\text{As}_{0.4}\text{P}_{0.6}$  shows better stability in ambient environment than BP (Figure 4a) after over 10 h of annealing and cooling in a vacuum. The degradation kinetics for BP and  $\text{As}_{0.4}\text{P}_{0.6}$  correspond to a monoexponential model,  $(1 - \exp(-\frac{t}{\tau}))$ . The coupling between the thermal and electrical phenomena in BP deteriorates relatively faster because of the photo-assisted oxygen degradation of the P-P bond [6]. After over 500 min of exposure to ambient conditions, the TEP of  $\text{As}_{0.4}\text{P}_{0.6}$  demonstrated stability, settling

approximately 1.4 times slower than BP (Table S2). Chemically modifying BP with As atoms to ensure oxygen sequestration has proven to ensure better stability in transport properties of interest. Figure 4b also shows the sustained stability of the four-probe resistance of  $\text{As}_{0.4}\text{P}_{0.6}$  over BP after exposure to air. The normalized resistance for BP shows a rapid drop after approximately 40 min of exposure while the resistance of  $\text{As}_{0.4}\text{P}_{0.6}$  decreases much slower. The resistance of BP and  $\text{As}_{0.4}\text{P}_{0.6}$  also fitted well with a monoexponential decay function as shown in Figure 4a. The metallic character of As also contributes to the stabilized electrical transport properties of  $\text{As}_x\text{P}_{1-x}$ . The normalized resistance for BP decays approximately four times faster than BP as shown in Table S3.

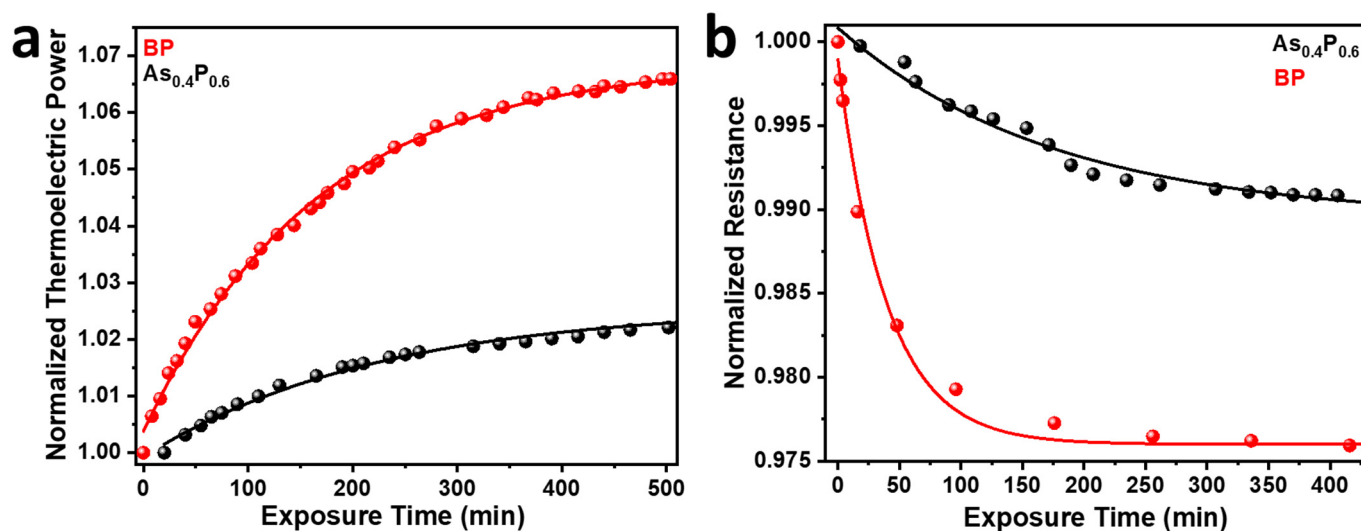


**Figure 4.** Results derived from electrical transport measurements of exposed samples after annealing. (a) Normalized TEP for  $\text{As}_{0.4}\text{P}_{0.6}$  and BP. (b) Normalized resistance for  $\text{As}_{0.4}\text{P}_{0.6}$  and BP.

The difference in degradation characteristics in Raman spectroscopy and electrical transport measurement data originates from the difference in experimental procedures. Raman studies were performed on samples that were already exposed to air (oxygen and moisture) and it reflects the long-term degradation properties showing longer time constants (days) shown in Table S1. However, TEP and resistance were studied right after they were exposed to air from their degassed states and the transport properties reflect changes in thermal and electrical properties with shorter time constants (minutes) shown in Tables S2 and S3. The discrepancy in the time constant values observed in resistance (Table S2) and TEP (Table S3) data is due to the grain boundary effects and other scattering events that only influence the resistance. The room temperature TEP for BP and  $\text{As}_{0.4}\text{P}_{0.6}$  were of  $250 \mu\text{V}/\text{K}$  and  $145 \mu\text{V}/\text{K}$ , respectively (Figure S4a). This confirms the dominance of hole concentrations (p-type) in these semiconductors. The corresponding room temperature four-probe resistances for BP and  $\text{As}_{0.4}\text{P}_{0.6}$  were  $0.27 \Omega$  and  $0.085 \Omega$ , respectively (Figure S4b).

In general, whenever a semiconductor is exposed to humid air, a charge transfer is expected between the adsorbed water film and the solid in a direction that tends to bring the Fermi energy ( $E_F$ ) of the material to an equilibrium with the electrochemical potential of the film. This is based on the electron exchange between the material and the aqueous redox couple  $\text{O}_2 + 4\text{H}^+ + 4\text{e}^- \rightleftharpoons 2\text{H}_2\text{O}$  [28]. All key components originate from normal humid air: the water film provides both a medium for the electrochemical reaction as well as the  $\text{O}_2$  and the  $\text{H}^+$  (the protons arise from acidity generated by  $\text{CO}_2$  that is present in air). Previously, this mechanism has been proposed and used to explain a long-standing problem of a curious phenomenon—undoped diamond—an exceedingly good insulator, showing substantial conductivity when exposed to air [20]. This mechanism has also been shown to play an important role in other carbon materials [29–32], as well as in inorganic materials, such as GaN and ZnO [33,34]. Reported values of the Fermi energy ( $E_F$ ) of carbon

solids, such as graphite, diamond, carbon nanotubes, and graphene are all well above the electrochemical potential of the oxygen redox couple in air ( $-5.3$  eV) [28]. Therefore, the redox couple can serve as an external acceptor and be responsible for  $E_F$  pinning and modified electrical properties of these materials [34,35].

Previous studies have reported the work function for BP to range from  $\sim 5.17$  eV for monolayer to  $\sim 4.58$  eV for tri-layer. This varies inversely with the number of BP layers [36]. The valence band edges of BP are above the  $O_2/O_2^-$  redox couple in air [6,14,27], alloying with As causes a shift in the Fermi level so that it approaches the redox potential of  $O_2/O_2^-$  as shown in Figure 5, which is consistent with the prediction that band bending (and charge transfer) will be minimal and the Fermi energy throughout the solid will be pinned close to that of the redox couple in the adsorbed water film. Yang et al. observed this phenomenon (i.e., Fermi level pinning) with Te-doped BP where ambient degradation was inhibited and Te-doped devices demonstrated impressive retained mobility of over  $200 \text{ cm}^2 \text{ v}^{-1} \text{ s}^{-1}$  [14].

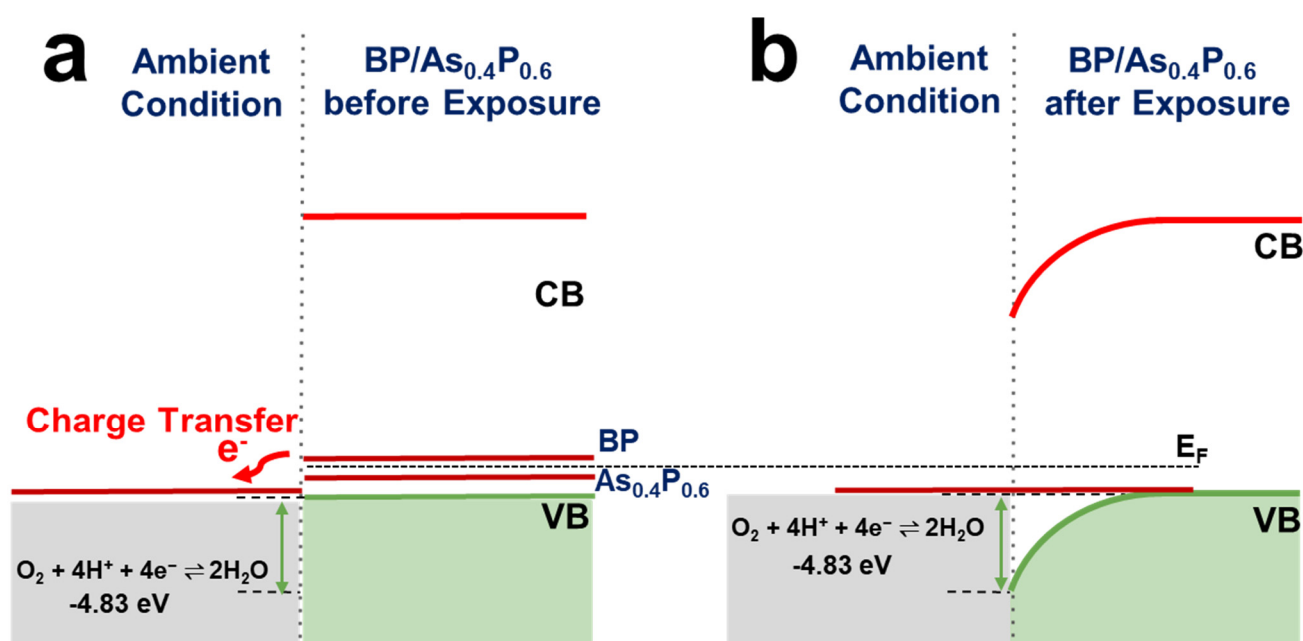


**Figure 5.** Band diagrams explaining the electron exchange between BP/ $As_xP_{1-x}$   $As_xP_{1-x}$  material systems and the aqueous redox couple (a) before and (b) after exposure to ambient conditions.

#### 4. Conclusions

The environmental stability of BP and  $As_xP_{1-x}$  was studied by evaluating their optical and electrical transport properties under controlled conditions. The Raman analysis of BP and  $As_xP_{1-x}$  when exposed to air indicated that BP degraded nearly three times faster than  $As_{0.6}P_{0.4}$ . This emphasizes that increasing the concentration of As atoms in BP improves its stability. The degradation times for BP,  $As_{0.2}P_{0.8}$ , and  $As_{0.4}P_{0.6}$  were recorded as 4, 5, and 11 days, respectively. Additionally, the electrical transport properties of  $As_{0.4}P_{0.6}$  and BP after being exposed to air showed that the thermal and electrical coupling between P-P in BP was improved through alloying with As atoms. The kinetics of the charge transfer-related evolution of electrical transport parameters followed exponential growth (TEP) and exponential decay (resistance) models, respectively. The TEP of  $As_{0.4}P_{0.6}$  stabilized slower than BP by 1.4 times, while BP's resistance decayed faster than  $As_{0.4}P_{0.6}$  by four times after being exposed to ambient conditions. The redox potential of  $As_xP_{1-x}$  is closer to the  $O_2/O_2^-$  ( $-4.5$  eV) compared to BP, leading to reduced charge transfer effects and degradation at the surface–water interface. Furthermore, when cooled and annealed samples of  $As_{0.4}P_{0.6}$  and BP were exposed to ambient conditions, it was determined that the normalized TEP and four-probe resistance of  $As_{0.4}P_{0.6}$  were relatively stable compared to BP.

**Supplementary Materials:** The following supporting information can be downloaded at: <https://www.mdpi.com/article/10.3390/chemengineering7020018/s1>, Figure S1: Degradation color maps highlighting the vanishing Raman modes of BP and  $\text{As}_{0.2}\text{P}_{0.8}$  as time progresses. (a) BP (b)  $\text{As}_{0.2}\text{P}_{0.8}$ ; Figure S2: Degradation of the peak intensities of P–P Raman vibration modes. (a)  $A_g^1$  (b)  $B_{2g}$  (c)  $A_g^2$ ; Figure S3: Peak positions for P–P Raman vibration modes. (a)  $A_g^1$  (b)  $B_{2g}$  (c)  $A_g^2$ ; Table S1: Decay function parameters for Raman spectra; Table S2: Growth function parameters for normalized thermoelectric power (TEP); Table S3: Decay function parameters for normalized resistance; Figure S4: Response of the electrical transport properties of BP and  $\text{As}_{0.4}\text{P}_{0.6}$  to heating and cooling. (a) TEP and (b) resistance.

**Author Contributions:** Conceptualization, J.B.J. and G.S.; methodology, U.O.A., D.V. and A.V.; validation, J.B.J., G.S. and U.O.A.; formal analysis, U.O.A. and D.V.; investigation, U.O.A.; data curation, U.O.A., D.V. and A.V.; writing—original draft preparation, U.O.A.; writing—review and editing, J.B.J. and G.S.; visualization, U.O.A.; supervision, J.B.J. and G.S.; project administration, J.B.J. and G.S.; funding acquisition, J.B.J. and G.S. All authors have read and agreed to the published version of the manuscript.

**Funding:** This work was supported by the U.S. Department of Energy, Office of Science, Basic Energy Sciences, under Award # DE-SC0019348.

**Institutional Review Board Statement:** Not applicable.

**Informed Consent Statement:** Not applicable.

**Data Availability Statement:** Not applicable.

**Conflicts of Interest:** The authors declare no conflict of interest.

## References

1. Artel, V.; Guo, Q.; Cohen, H.; Gasper, R.; Ramasubramaniam, A.; Xia, F.; Naveh, D. Protective molecular passivation of black phosphorus. *NPJ 2D Mater. Appl.* **2017**, *1*, 6. [[CrossRef](#)]
2. Yau, S.-L.; Moffat, T.P.; Bard, A.J.; Zhang, Z.; Lerner, M.M. STM of the (010) surface of orthorhombic phosphorus. *Chem. Phys. Lett.* **1992**, *198*, 383–388. [[CrossRef](#)]
3. Castellanos-Gomez, A.; Vicarelli, L.; Prada, E.; Island, J.O.; Narasimha-Acharya, K.; Blanter, S.I.; Groenendijk, D.J.; Buscema, M.; Steele, G.A.; Alvarez, J. Isolation and characterization of few-layer black phosphorus. *2D Mater.* **2014**, *1*, 025001. [[CrossRef](#)]
4. Sang, D.K.; Wang, H.; Guo, Z.; Xie, N.; Zhang, H. Recent developments in stability and passivation techniques of phosphorene toward next-generation device applications. *Adv. Funct. Mater.* **2019**, *29*, 1903419. [[CrossRef](#)]
5. Hyun, C.; Kim, J.H.; Lee, J.-Y.; Lee, G.-H.; Kim, K.S. Atomic scale study of black phosphorus degradation. *RSC Adv.* **2020**, *10*, 350–355. [[CrossRef](#)] [[PubMed](#)]
6. Favron, A.; Gaufrès, E.; Fossard, F.; Phaneuf-L'Heureux, A.-L.; Tang, N.Y.W.; Lévesque, P.L.; Loiseau, A.; Leonelli, R.; Francoeur, S.; Martel, R. Photooxidation and quantum confinement effects in exfoliated black phosphorus. *Nat. Mater.* **2015**, *14*, 826–832. [[CrossRef](#)]
7. Gamage, S.; Li, Z.; Yakovlev, V.S.; Lewis, C.; Wang, H.; Cronin, S.B.; Abate, Y. Nanoscopy of black phosphorus degradation. *Adv. Mater. Interfaces* **2016**, *3*, 1600121. [[CrossRef](#)]
8. Li, Q.; Zhou, Q.; Shi, L.; Chen, Q.; Wang, J. Recent advances in oxidation and degradation mechanisms of ultrathin 2D materials under ambient conditions and their passivation strategies. *J. Mater. Chem. A* **2019**, *7*, 4291–4312. [[CrossRef](#)]
9. Abate, Y.; Akinwande, D.; Gamage, S.; Wang, H.; Snure, M.; Poudel, N.; Cronin, S.B. Recent progress on stability and passivation of black phosphorus. *Adv. Mater.* **2018**, *30*, 1704749. [[CrossRef](#)]
10. Wood, J.D.; Wells, S.A.; Jariwala, D.; Chen, K.-S.; Cho, E.; Sangwan, V.K.; Liu, X.; Lauhon, L.J.; Marks, T.J.; Hersam, M.C. Effective Passivation of Exfoliated Black Phosphorus Transistors against Ambient Degradation. *Nano Lett.* **2014**, *14*, 6964–6970. [[CrossRef](#)]
11. Kim, J.-S.; Liu, Y.; Zhu, W.; Kim, S.; Wu, D.; Tao, L.; Dodabalapur, A.; Lai, K.; Akinwande, D. Toward air-stable multilayer phosphorene thin-films and transistors. *Sci. Rep.* **2015**, *5*, 8989. [[CrossRef](#)]
12. Uk Lee, H.; Lee, S.C.; Won, J.; Son, B.-C.; Choi, S.; Kim, Y.; Park, S.Y.; Kim, H.-S.; Lee, Y.-C.; Lee, J. Stable semiconductor black phosphorus (BP)@ titanium dioxide ( $\text{TiO}_2$ ) hybrid photocatalysts. *Sci. Rep.* **2015**, *5*, srep08691. [[CrossRef](#)]
13. Avsar, A.; Vera-Marun, I.J.; Tan, J.Y.; Watanabe, K.; Taniguchi, T.; Castro Neto, A.H.; Ozyilmaz, B. Air-stable transport in graphene-contacted, fully encapsulated ultrathin black phosphorus-based field-effect transistors. *ACS Nano* **2015**, *9*, 4138–4145. [[CrossRef](#)] [[PubMed](#)]
14. Yang, B.; Wan, B.; Zhou, Q.; Wang, Y.; Hu, W.; Lv, W.; Chen, Q.; Zeng, Z.; Wen, F.; Xiang, J. Te-doped black phosphorus field-effect transistors. *Adv. Mater.* **2016**, *28*, 9408–9415. [[CrossRef](#)] [[PubMed](#)]
15. Karki, B.; Rajapakse, M.; Sumanasekera, G.U.; Jasinski, J.B. Structural and Thermoelectric Properties of Black Arsenic–Phosphorus. *ACS Appl. Energy Mater.* **2020**, *3*, 8543–8551. [[CrossRef](#)]

16. Han, R.; Feng, S.; Sun, D.-M.; Cheng, H.-M. Properties and photodetector applications of two-dimensional black arsenic phosphorus and black phosphorus. *Sci. China Inf. Sci.* **2021**, *64*, 140402. [[CrossRef](#)]
17. Liang, J.; Hu, Y.; Zhang, K.; Wang, Y.; Song, X.; Tao, A.; Liu, Y.; Jin, Z. 2D layered black arsenic-phosphorus materials: Synthesis, properties, and device applications. *Nano Res.* **2021**, *15*, 3737–3752. [[CrossRef](#)]
18. Tsai, Y.-C.; Bayram, C. Structural and electronic properties of hexagonal and cubic phase AlGaInN alloys investigated using first principles calculations. *Sci. Rep.* **2019**, *9*, 6583. [[CrossRef](#)]
19. Xu, Y.; Shi, Z.; Shi, X.; Zhang, K.; Zhang, H. Recent progress in black phosphorus and black-phosphorus-analogue materials: Properties, synthesis and applications. *Nanoscale* **2019**, *11*, 14491–14527. [[CrossRef](#)]
20. Chakrapani, V.; Angus, J.C.; Anderson, A.B.; Wolter, S.D.; Stoner, B.R.; Sumanasekera, G.U. Charge transfer equilibria between diamond and an aqueous oxygen electrochemical redox couple. *Science* **2007**, *318*, 1424–1430. [[CrossRef](#)]
21. Desai, S.; Rivera, J.; Jalilian, R.; Hewaparakrama, K.; Sumanasekera, G. Studies of electronic distribution in potassium-doped mats of single-walled carbon nanotubes, double-walled carbon nanotubes, and peapods. *J. Appl. Phys.* **2008**, *104*, 013707. [[CrossRef](#)]
22. Akhtar, M.; Zhang, C.; Rajapakse, M.; Musa, M.R.K.; Yu, M.; Sumanasekera, G.; Jasinski, J.B. Bilayer phosphorene under high pressure: In situ Raman spectroscopy. *Phys. Chem. Chem. Phys.* **2019**, *21*, 7298–7304. [[CrossRef](#)]
23. Köpf, M.; Eckstein, N.; Pfister, D.; Grotz, C.; Krüger, I.; Greiwe, M.; Hansen, T.; Kohlmann, H.; Nilges, T. Access and in situ growth of phosphorene-precursor black phosphorus. *J. Cryst. Growth* **2014**, *405*, 6–10. [[CrossRef](#)]
24. Rajapakse, M.; Musa, R.; Abu, U.O.; Karki, B.; Yu, M.; Sumanasekera, G.; Jasinski, J.B. Electrochemical Li intercalation in black phosphorus: In situ and ex situ studies. *J. Phys. Chem. C* **2020**, *124*, 10710–10718. [[CrossRef](#)]
25. Abu, U.O.; Musa, M.R.K.; Rajapakse, M.; Karki, B.; Vithanage, D.; Yu, M.; Sumanasekera, G.; Jasinski, J.B. Vapor-Phase Intercalation of Cesium into Black Phosphorous. *J. Phys. Chem. C* **2021**, *125*, 27440–27448. [[CrossRef](#)]
26. Abu, U.O.; Akter, S.; Nepal, B.; Pitton, K.A.; Guiton, B.S.; Strachan, D.R.; Sumanasekera, G.; Wang, H.; Jasinski, J.B. Ultra-Narrow Phosphorene Nanoribbons Produced by Facile Electrochemical Process. *Adv. Sci.* **2022**, *9*, 2203148. [[CrossRef](#)] [[PubMed](#)]
27. Gómez-Pérez, J.; Barna, B.; Tóth, I.Y.; Kónya, Z.; Kukovecz, A.K. Quantitative tracking of the oxidation of black phosphorus in the few-layer regime. *ACS Omega* **2018**, *3*, 12482–12488. [[CrossRef](#)]
28. Lide, D.R. *CRC Handbook of Chemistry and Physics*; CRC Press: Boca Raton, FL, USA, 2004; Volume 85.
29. Qi, D.; Chen, W.; Gao, X.; Wang, L.; Chen, S.; Loh, K.P.; Wee, A.T. Surface transfer doping of diamond (100) by tetrafluoro-tetracyanoquinodimethane. *J. Am. Chem. Soc.* **2007**, *129*, 8084–8085. [[CrossRef](#)] [[PubMed](#)]
30. Sque, S.J.; Jones, R.; Briddon, P.R. The transfer doping of graphite and graphene. *Phys. Status Solidi* **2007**, *204*, 3078–3084. [[CrossRef](#)]
31. Suzuki, S.; Bower, C.; Watanabe, Y.; Zhou, O. Work functions and valence band states of pristine and Cs-intercalated single-walled carbon nanotube bundles. *Appl. Phys. Lett.* **2000**, *76*, 4007–4009. [[CrossRef](#)]
32. Suzuki, S.; Watanabe, Y.; Homma, Y.; Fukuba, S.-Y.; Heun, S.; Locatelli, A. Work functions of individual single-walled carbon nanotubes. *Appl. Phys. Lett.* **2004**, *85*, 127–129. [[CrossRef](#)]
33. Wang, Q.; Puntambekar, A.; Chakrapani, V. Co-adsorption of water and oxygen on GaN: Effects of charge transfer and formation of electron depletion layer. *J. Chem. Phys.* **2017**, *147*, 104703. [[CrossRef](#)] [[PubMed](#)]
34. Chakrapani, V.; Pendyala, C.; Kash, K.; Anderson, A.B.; Sunkara, M.K.; Angus, J.C. Electrochemical pinning of the Fermi level: Mediation of photoluminescence from gallium nitride and zinc oxide. *J. Am. Chem. Soc.* **2008**, *130*, 12944–12952. [[CrossRef](#)]
35. Chandel, M.; Thakur, M.; Sharma, A.; Pathania, D.; Kumar, A.; Singh, L. Chlorophyll sensitized (BiO)<sub>2</sub>CO<sub>3</sub>/CdWO<sub>4</sub>/rGO nano-hybrid assembly for solar assisted photo-degradation of chlorzoxazone. *Chemosphere* **2022**, *305*, 135472. [[CrossRef](#)] [[PubMed](#)]
36. Cai, Y.; Zhang, G.; Zhang, Y.-W. Layer-dependent band alignment and work function of few-layer phosphorene. *Sci. Rep.* **2014**, *4*, 6677. [[CrossRef](#)]

**Disclaimer/Publisher’s Note:** The statements, opinions and data contained in all publications are solely those of the individual author(s) and contributor(s) and not of MDPI and/or the editor(s). MDPI and/or the editor(s) disclaim responsibility for any injury to people or property resulting from any ideas, methods, instructions or products referred to in the content.